

Three-dimensional lattice model for coupling of fracture and mass transport

Peter Grassl^{1*} and John E. Bolander²

¹ School of Engineering, University of Glasgow, Glasgow, UK

² Department of Civil and Environmental Engineering, University of California, Davis, U.S.A.

*Corresponding author: Email: peter.grassl@glasgow.ac.uk, Phone: +44 141 330 5208

Abstract

Dual lattices are combined to model the coupling of fracture and mass transport in quasi-brittle materials. Elemental connectivity within the mechanical lattice, representing elasticity and fracture, is defined by the Delaunay tessellation of a random set of points. The connectivity of conduit elements within the transport lattice is defined by the Voronoi tessellation of the same set of points. The enforcement of boundary conditions is facilitated by a novel procedure for discretising the domain boundaries. The use of dual lattices provides a natural means for simulating transport along cracks and from the crack surfaces into the bulk material. The properties of conduit elements evolve with the crack opening values of neighbouring mechanical elements. Through benchmark comparisons involving non-stationary flow and fracture, the proposed dual lattice approach is shown to be objective with respect to element size and orientation.

1 Introduction

The coupling of fracture and mass transport affects physical processes that govern many engineering applications, such as deterioration of construction materials, hydraulic fracturing for oil and gas extraction, and performance of waste barriers. In these applications, it is important to consider the influence of fracture induced pathways for the ingress of fluids. Modelling the discrete crack formations, and the mass transport along these cracks and through the surrounding uncracked material, is challenging. Models for this coupling can be entirely based on continuum mechanics [14], or continuum mechanics combined with a discrete representations of cracks [19, 22, 23, 6, 28]. Alternatively, discrete approaches have been proposed to model these processes [20, 7, 15, 26, 8, 25, 12, 13].

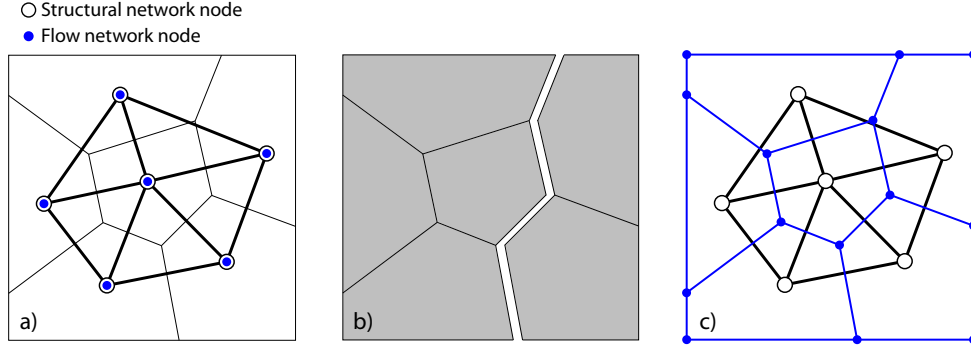


Figure 1: Lattice models for coupled problems: a) common approach in which the mechanical and flow network nodes are coincident. Both mechanical and flow elements are on the Delaunay edges; b) simulated crack in mechanical network; and c) improved approach in which flow elements are on the Voronoi edges and therefore aligned with potential cracks.

One lattice approach, based on the Delaunay tessellation of an unstructured set of points, has been shown to be suitable for modelling fracture [4, 5, 10, 9] and mass transport [3], providing accurate and mesh insensitive results. The physical processes are modelled by a multi-dimensional network of one-dimensional elements, which are placed on the edges of the Delaunay tessellation (Fig. 1a); the element properties are determined by the corresponding Voronoi tessellation. The nodes representing the mechanical problem are coincident with those representing flow related quantities. This element sharing of nodal sites facilitates coupled-field analyses prior to cracking. Upon crack formation, however, the flow elements are oriented perpendicular to the simulated crack path, which runs along the boundaries of the Voronoi cells (Fig. 1b). This misalignment of the flow elements with the crack path complicates the modelling of crack-assisted flow and its dependence on crack opening. To resolve this deficiency, several researchers [15, 8, 21, 1, 12] have placed conduit elements on the Voronoi edges, whereas the mechanical elements remain on the Delaunay edges (Fig. 1c). With this dual lattice approach, the influence of fracture on transport is more naturally represented, since the conduit elements are aligned with the potential crack directions.

This work extends the capabilities of the dual-lattice approach for modelling coupled fracture and mass transport. In particular, three-dimensional models are developed and used to study cases of non-stationary flow, fracture, and the coupling of these two processes. The enforcement of boundary conditions is facilitated by a novel routine for discretising the domain boundaries. Based on the geometric relationship between the Delaunay and Voronoi tessellations, a procedure

is given for coupling the displacement and flow fields, such that flow along cracks is dependent on crack opening. The two-way coupling of field quantities (i.e., including the dependence of mechanical behaviour on the flow field [12]) is a natural extension of this work. Comparisons are made with benchmark problems to validate model accuracy and objectivity of the results with respect to mesh size and orientation.

2 Modelling approach

2.1 Discretisation

The dual lattice approach is based on the Voronoi and Delaunay tessellations of a set of points placed randomly within the domain. The points are placed sequentially while enforcing a minimum distance d_{\min} between all points; trial points that fail the minimum distance criterion are rejected. The Delaunay tessellation decomposes the domain into tetrahedra whose vertices coincide with the randomly placed points; the Voronoi tessellation divides the domain into polyhedra associated with the random points [16]. These geometrical arrangements of Delaunay and Voronoi tessellations are used to define the mechanical and transport elements. Figure 2(a) shows a Delaunay tetrahedron and the Voronoi facet associated with Delaunay edge $i - j$. The mechanical elements are placed on the Delaunay edges with their mid-cross-sections defined by the facets of the Voronoi polyhedra (Figure 2(b)). Analogous to the mechanical lattice, the transport elements are placed on the edges of the Voronoi polyhedra, with their cross-sections formed by the facets of the Delaunay tetrahedra (Figure 2(c)).

The discretisation of boundaries of the domain requires special attention. The procedure used in this work is illustrated in Figure 3. Prior to the sequential, random filling of points within the domain, points are placed randomly on the domain surface. The minimum distance criterion is enforced during the placement of all of these points. Each interior point is then mirrored with respect to all surfaces of the domain, similar to the procedure of Yip et al. [29]. The difference lies in the positioning of points on the domain surfaces, which form Voronoi facets that traverse the domain surfaces as shown in Figure 3(a). In constructing the flow lattice, the Voronoi edges within the domain are retained. For edges that cross a surface, only the portion within the

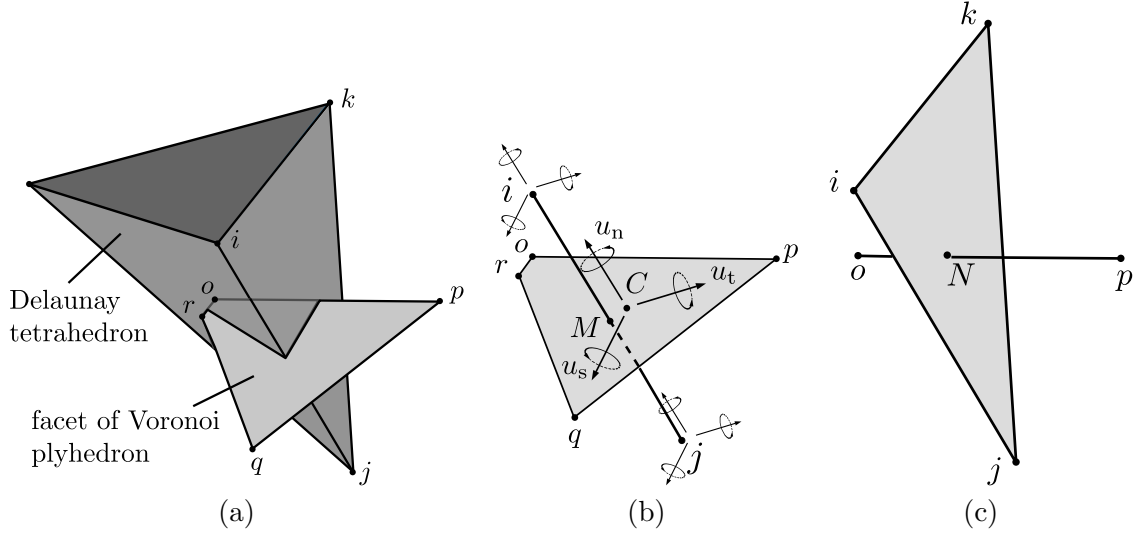


Figure 2: Spatial arrangement of mechanical and transport elements of the 3D hydro-mechanical lattice approach: a) Geometrical relationship between Delaunay and Voronoi tessellations, (b) mechanical element with cross-section defined by the associated Voronoi facet, (c) transport element with cross-section defined by the associated Delaunay facet.

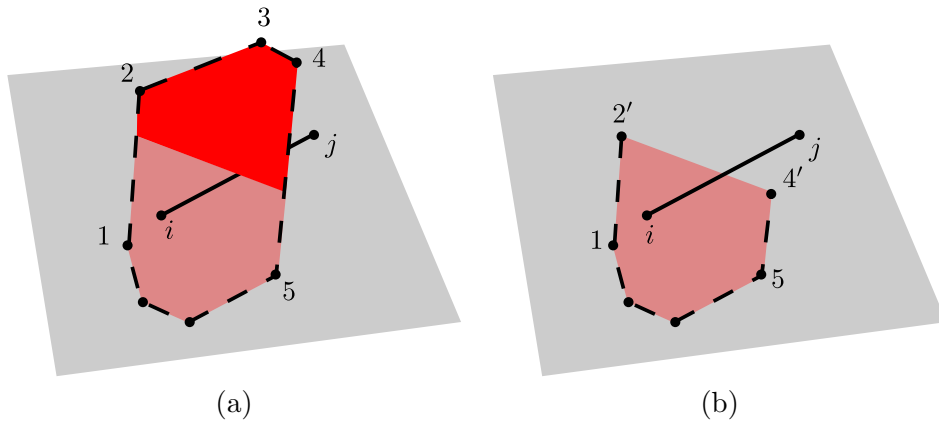


Figure 3: Discretisation of domain boundaries. (a) Voronoi facet of Delaunay edge $i-j$ located on the surface of the domain after initial tessellation. (b) Modified arrangement used for definition of transport nodes and elements.

domain is kept. For example, edges 1-2 and 4-5 become edges 1-2' and 4'-5, respectively, where nodes 2' and 4' lie on the surface (Fig. 3(b)). These truncated edges define conduit elements that are perpendicular to the surface. The modified set of Voronoi edges defines the mid-section of the mechanical element associated with nodes i and j .

Information exchange between the mechanical and transport lattices is based on the geometrical relationship between neighbouring elements. Herein, a one-way coupling is considered, in which crack openings supplied by the mechanical lattice affect conductivity of the associated conduit elements. Details regarding this coupling are provided in section 2.3.

2.2 Mechanical model

All geometrical information of the lattice element is contained in the element formulation. In this way, the constitutive model depends only on properties of the material represented by the element. This structure is preferred over one that incorporates geometrical information in the constitutive model, since it allows for easier comparisons with continuum constitutive models reported in the literature. For an elastic constitutive model, the present mechanical element is identical to the one described in Berton and Bolander [2].

For the mechanical element in Figure 2(b), each node has 3 translational and 3 rotational degrees of freedom. These degrees of freedom are used to determine displacement discontinuities at point C by means of

$$\mathbf{u}_C = \mathbf{B}\mathbf{u}_e \quad (1)$$

where $\mathbf{u}_C = \{u_n, u_s, u_t, \phi_n, \phi_s, \phi_t\}^T$ are the displacement discontinuities, and $\mathbf{u}_e = \{u_{xi}, u_{yi}, u_{zi}, \phi_{xi}, \phi_{yi}, \phi_{zi}, u_{xj}, u_{yj}, u_{zj}, \phi_{xj}, \phi_{yj}, \phi_{zj}\}^T$ are the degrees of freedom at nodes i and j in the local coordinate system, as shown in Figure 2(b). At the centroid C of the mid-cross-section, the direction n is parallel to the axis of the element, and s and t are chosen as the two principal axes of the mid-cross-section. Furthermore, in Eq. (1), the matrix \mathbf{B} is

$$\mathbf{B} = \begin{bmatrix} \mathbf{I} & \mathbf{B}_1 & \mathbf{I} & \mathbf{B}_2 \\ 0 & -\mathbf{B}_3 & 0 & \mathbf{B}_3 \end{bmatrix} \quad (2)$$

where the submatrices \mathbf{B}_1 , \mathbf{B}_2 and \mathbf{B}_3 are

$$\mathbf{B}_1 = \begin{bmatrix} 0 & -e_t & e_s \\ e_t & 0 & -h/2 \\ -e_s & h/2 & 0 \end{bmatrix} \quad (3)$$

,

$$\mathbf{B}_2 = \begin{bmatrix} 0 & e_t & -e_s \\ -e_t & 0 & -h/2 \\ e_s & h/2 & 0 \end{bmatrix} \quad (4)$$

and

$$\mathbf{B}_3 = \begin{bmatrix} \sqrt{I_p/A} & 0 & 0 \\ 0 & \sqrt{I_1/A} & 0 \\ 0 & 0 & \sqrt{I_2/A} \end{bmatrix} \quad (5)$$

In Eqs. (4) and (5), e_s and e_t are the eccentricities between the midpoint of the lattice element and the centroid C in the directions s and t of the local coordinate system, respectively. In addition, h is the length of the element, A is the cross-sectional area, I_p is the polar second moment of area and I_1 and I_2 are the two principal second moments of area of the mid-cross-section. The displacement jump \mathbf{u}_C in Eq. (1) is transformed into strains $\boldsymbol{\varepsilon} = \{\varepsilon_n, \varepsilon_s, \varepsilon_t, \varepsilon_\phi, \varepsilon_\psi, \varepsilon_\theta\}^T = \mathbf{u}_C/h$. In the local coordinate system, shown in Figure 2(b), the stiffness matrix is:

$$\mathbf{K}_e = \frac{A}{h} \mathbf{B}^T \mathbf{D} \mathbf{B} \quad (6)$$

where \mathbf{D} is the constitutive matrix of the material, which for the case of linear elasticity is a diagonal matrix of the form $\mathbf{D} = \text{diag}\{E, \gamma E, \gamma E, E, E, E\}$. Here, the model parameter γ , which controls the ratio of shear and normal stiffness, is used to control the effective Poisson's ratio of the continuum approximated by an irregular arrangement of elements. Whereas $\gamma = 1$ provides Poisson's ratio equal to zero, it has the advantage of rendering the mechanical lattice elastically homogeneous under uniform modes of straining. For this reason, $\gamma = 1$ is used herein.

The inelastic mechanical response of the material during fracture is described by a scalar damage model of the form

$$\boldsymbol{\sigma} = (1 - \omega) \mathbf{D}_e \boldsymbol{\varepsilon} = (1 - \omega) \bar{\boldsymbol{\sigma}} \quad (7)$$

where ω is a damage parameter and $\bar{\sigma}$ is the effective stress, which is transferred by the undamaged material. The value of ω is a function of the history variable κ_d , which is, in turn, determined by the loading function

$$f(\boldsymbol{\varepsilon}, \kappa_d) = \varepsilon_{\text{eq}}(\boldsymbol{\varepsilon}) - \kappa_d \quad (8)$$

and the loading-unloading conditions

$$f \leq 0, \quad \dot{\kappa}_d \geq 0, \quad \dot{\kappa}_d f = 0 \quad (9)$$

The equivalent strain

$$\varepsilon_{\text{eq}}(\varepsilon_n, \varepsilon_s, \varepsilon_t) = \frac{1}{2}\varepsilon_0(1-c) + \sqrt{\left(\frac{1}{2}\varepsilon_0(c-1) + \varepsilon_n\right)^2 + \frac{c\gamma^2(\varepsilon_s + \varepsilon_t)^2}{q^2}} \quad (10)$$

corresponds to an ellipsoidal stress envelope in the nominal stress space. For pure tensile loading, the nominal stress is limited by the tensile strength $f_t = E\varepsilon_0$. For pure shear and pure compression, the nominal stress is limited by the shear strength $f_q = qf_t$ and the compressive strength $f_c = cf_t$, respectively.

The damage function is determined by using an exponential stress-crack law in uniaxial tension of the form

$$\sigma = f_t \exp\left(-\frac{w_c}{w_f}\right) \quad (11)$$

where $w_c = \omega h \varepsilon$ is the crack opening under monotonic uniaxial tension and ε is the uniaxial strain. This crack opening is the first component of the crack opening vector $\mathbf{w}_c = \omega h \boldsymbol{\varepsilon}$, which is used for the coupling of the mechanical and mass transport model. The stress-strain law in Eq. (11) can also be expressed in terms of the damage variable as

$$\sigma = (1 - \omega) E \varepsilon \quad (12)$$

Comparing the right-hand sides of Eqs. (11) and (12), and replacing ε by κ_d , since a monotoni-

cally increasing tensile strain is assumed, the nonlinear equation

$$(1 - \omega) \kappa_d = \varepsilon_0 \exp \left(-\frac{\omega h \kappa_d}{w_f} \right) \quad (13)$$

is obtained from which the damage parameter ω can be determined iteratively using a Newton method. In Eq. (11), parameter w_f determines the initial slope of the softening curve and is related to the meso-level fracture energy $G_{ft} = f_t w_f$. The present damage constitutive model used here is conceptually similar to that presented in [17]. However, a more complex equivalent strain formulation involving the additional parameter c was required in the present study, since the compressive strength of concrete is significantly greater than its tensile strength. For $c = 1$ the original formulation proposed in [17] is obtained.

2.3 Transport model

For the transport part of the model, a 3D network of 1D conduit elements is used to discretise the nonstationary flow equation

$$\frac{\partial P_c}{\partial t} - \text{div} (\alpha \text{grad } P_c) = 0 \quad (14)$$

subject to

$$P_c = g(\mathbf{x}) \quad \text{on } \Gamma_1 \quad (15)$$

and

$$f = -\frac{\partial P_c}{\partial \mathbf{n}} \quad \text{on } \Gamma_2 \quad (16)$$

Here, P_c is the capillary suction, t is the time, α is the conductivity, f is the outward flux normal to the boundary (\mathbf{n} -direction) and \mathbf{x} is the position in the domain Ω . Furthermore, Γ_1 and Γ_2 are the boundary segments with prescribed suction and normal traction, respectively. The discrete form of Eq. (14) for a 1D-conduit element is

$$\mathbf{C}_e \frac{\partial \mathbf{P}_c}{\partial t} - \boldsymbol{\alpha}_e \mathbf{P}_c = \mathbf{f} \quad (17)$$

where $\boldsymbol{\alpha}_e$ and \mathbf{C}_e are the 1D element conductivity and capacity matrix, respectively, \mathbf{f} are the external fluxes, and the degrees of freedom of the conduit elements are the capillary suction

$\mathbf{P}_c = (P_{c1}, P_{c2})^T$ (Fig. 2b) [3]. The capacity matrix \mathbf{C}_e is

$$\mathbf{C}_e = c \frac{A_t h_t}{12} \begin{pmatrix} 2 & 1 \\ 1 & 2 \end{pmatrix} \quad (18)$$

where c is the capacity of the material, A_t is the cross-sectional area of the tetrahedron face associated with the conduit element (Fig. 4) and h_t is the length of the conduit element.

The conductivity matrix is defined as

$$\boldsymbol{\alpha}_e = \frac{A_t}{h_t} \alpha \begin{pmatrix} 1 & -1 \\ -1 & 1 \end{pmatrix} \quad (19)$$

where α is the conductivity of the material, which is the sum of two components

$$\alpha = \alpha_0 + \alpha_c \quad (20)$$

where α_0 is the initial conductivity of the undamaged material and α_c is the change of the conductivity due to fracture.

In the present example, the lattice approach is applied to mass transport in a general unsaturated geomaterial using techniques introduced originally for soils [24], but also applied to other geomaterials, such as concrete [11]. The conductivity of the undamaged material α_0 is defined as

$$\alpha_0 = \frac{\rho \kappa}{\mu} \kappa_r(S) \quad (21)$$

where ρ is the density of the fluid, μ is the viscosity, κ is the intrinsic permeability and κ_r is the relative permeability as a function of the degree of saturation. This degree of saturation is defined as

$$S = \frac{\theta - \theta_r}{\theta_s - \theta_r} \quad (22)$$

with the moisture content θ , the residual moisture content θ_r and the saturated moisture content θ_s of the specific geomaterial. Furthermore, the relative permeability κ_r is

$$\kappa_r(S) = \sqrt{S} \left(1 - \left(1 - S^{1/m} \right)^m \right)^2 \quad (23)$$

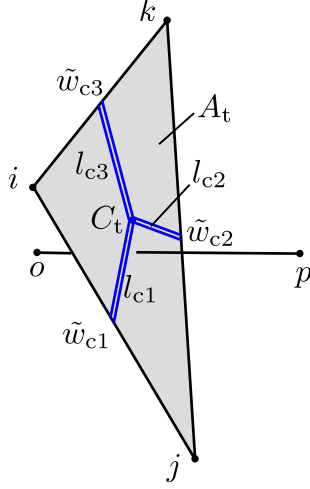


Figure 4: Influence of cracking on transport.

where m is a model parameter. The saturation is related to the capillary suction as

$$S(P_c) = \left(1 + \left(\frac{P_c}{a} \right)^{\frac{1}{1-m}} \right)^{-m} \quad (24)$$

where a is another model parameter.

The second term in Eq. (20) describes the influence of fracture on conductivity. It is defined as

$$\alpha_c = \xi \frac{\rho}{12\mu A_t} \sum_{i=1}^3 \tilde{w}_{ci}^3 l_{ci} \quad (25)$$

where \tilde{w}_{ci} and l_{ci} are the equivalent crack openings and crack lengths (see Figure 4) of neighbouring mechanical elements, which are located on the edges of the cross-section, and ξ is a tortuosity factor. For instance, for the transport element $o - p$ shown in Figure 4, three mechanical elements ($i - k$, $k - j$ and $i - j$) are positioned at the border of the cross-section of the transport element. Thus, the conductivity will be influenced by these three elements according to Eq. (25) in proportion to their equivalent crack widths and the crack lengths. This crack length is defined as length from the midpoint of the mechanical element to the centroid C_t of the transport element cross-section.

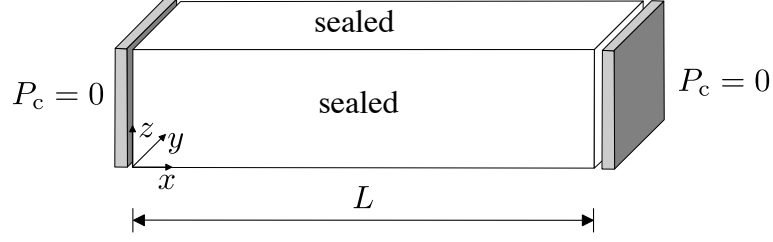


Figure 5: Geometry and boundary conditions for the nonstationary flow benchmark.

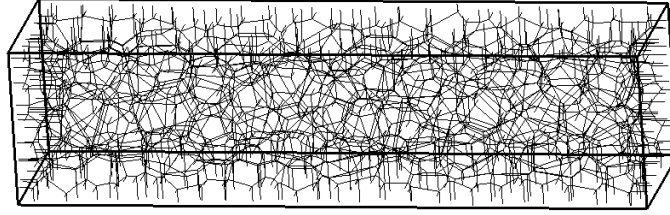


Figure 6: Coarse lattice for the transport analysis.

3 Analyses

3.1 Transport analysis

In the proposed coupled lattice approach, the transport elements are placed on the edges of the Voronoi polyhedra, which differs from the commonly used approach in which the elements are located at the edges of the Delaunay tetrahedra [3]. A benchmark for nonstationary mass transport is used to investigate the accuracy of this discretisation scheme [3, 21]. The geometry and boundary conditions of the benchmark are shown in Figure 5. The two ends of the specimen are subjected to zero pressure whereas all other boundaries are considered to be sealed. For this test, a special case of the constitutive model presented in Section 2.3 has been used by assuming the conductivity and capacity to be constant with values of $\alpha = 1$ and $c = 1$. The initial condition at all nodes is $P_c(x, t) = P_0 \sin\left(\frac{\pi x}{L}\right)$

Three transport lattices with minimum distances between Delaunay vertices of $d_{\min}/L = 0.06, 0.045$ and 0.03 are used. The coarse mesh with $d_{\min}/L = 0.06$ is shown in Figure 6. The analytical solution for this benchmark is $P_c = P_0 \sin\left(\frac{\pi x}{L}\right) \exp\left(-\frac{\pi^2}{L^2}t\right)$.

The pressure distributions for four time steps and the three different mesh sizes are shown in

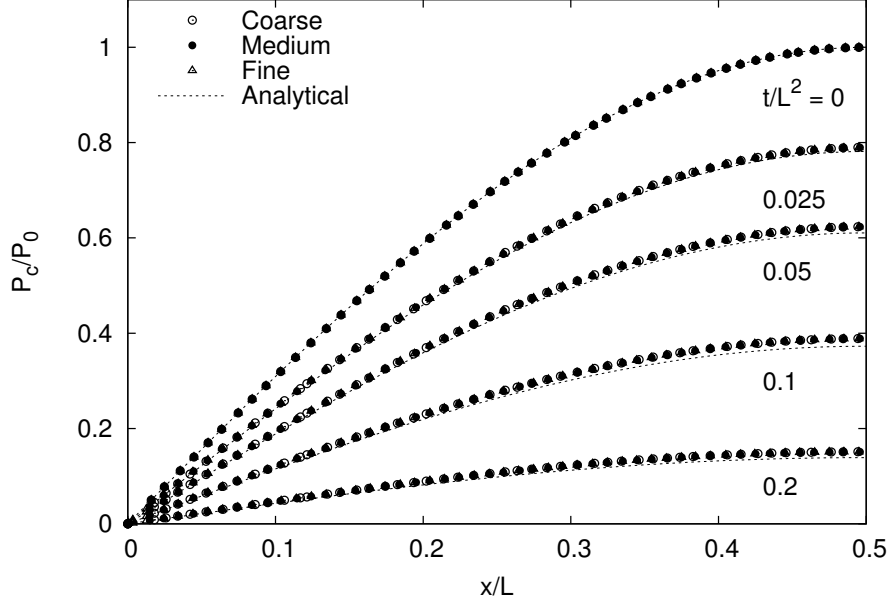


Figure 7: Pressure distributions due to non-stationary transport.

Figure 7 for a symmetric portion of the model. For comparing the lattice results with the analytical results, the vertices were divided into groups with respect to their x -coordinate. For each group of vertices the mean of the x -coordinate and unknown are presented. The Voronoi-edge based mesh agrees well with the analytical solution of the pressure distribution without exhibiting any mesh dependence. Any differences between the numerical and analytical solution originate from the time discretisation, rather than the spatial discretisation.

3.2 Coupled mechanical-transport benchmark

In the second benchmark, the mechanical and transport models are coupled. Firstly, a double cantilever beam is used to assess the capability of the mechanical model to describe fracture without any pathological mesh dependence. Then, fluid transport through the fractured specimen at an intermediate loading stage of the mechanical analysis is modelled for different lattice element sizes. The geometry and loading setup for the mechanical and transport tests are shown in Figure 8(a) and (b), respectively. For the mechanical analysis, the load is applied at $x = 0.25L$.

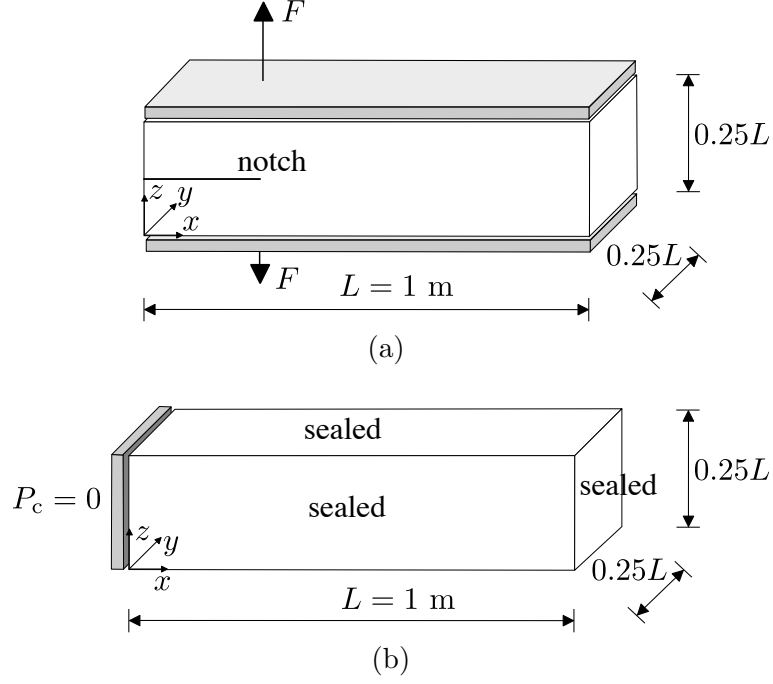


Figure 8: Geometry and loading setup of the mechanical and transport benchmark.

As for the transport component of the analyses, three lattices with minimum distances between Delaunay vertices of $d_{\min}/L = 0.06$, 0.045 and 0.03 are considered. The coarsest mesh with $d_{\min}/L = 0.06$ is shown in Figure 9 for mechanical and transport analysis, respectively. As noted earlier, conduit elements local to the model surfaces are perpendicular to the surfaces. The input parameters for the mechanical constitutive model are $E = 30$ GPa, $e_0 = 0.0001$ and $w_f = 0.04$ mm, which are representative of concrete materials. A notch of length $0.25L$ is introduced by reducing the peak strain threshold ε_0 of elements crossing the notch to 1% of the original value.

The load-displacement curves from the mechanical benchmark for the three lattices are shown in Figure 10. There is little difference between the responses obtained with the three meshes. Fracture is indicated by shading the mid-cross-sections of elements in which the equivalent crack opening has reached a threshold value. The mid-cross-sections of elements with damage corresponding to an equivalent crack opening $\tilde{w}_c > 10 \mu\text{m}$ are shown in Figure 11 for the three different lattices at a load point displacement of $\delta = 0.15$ mm in Figure 10.

The transport lattice uses the same geometry as in the nonstationary flow test in Section 3.1.

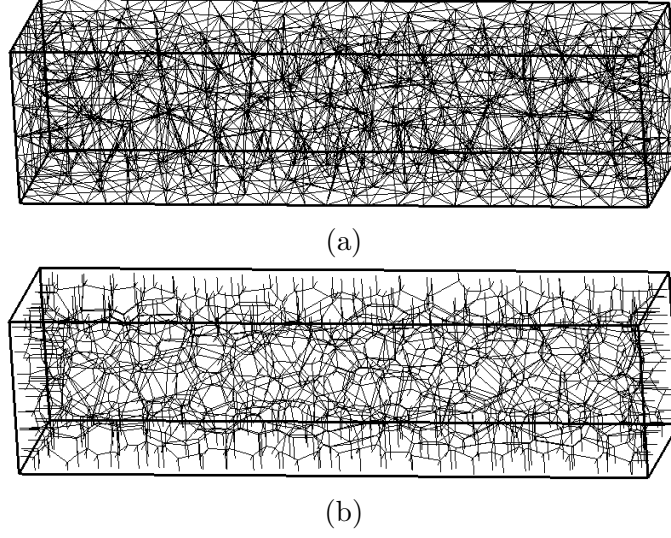


Figure 9: The coarse dual lattices ($d_{\min}/L = 0.06$) for (a) mechanical and (b) transport analysis.

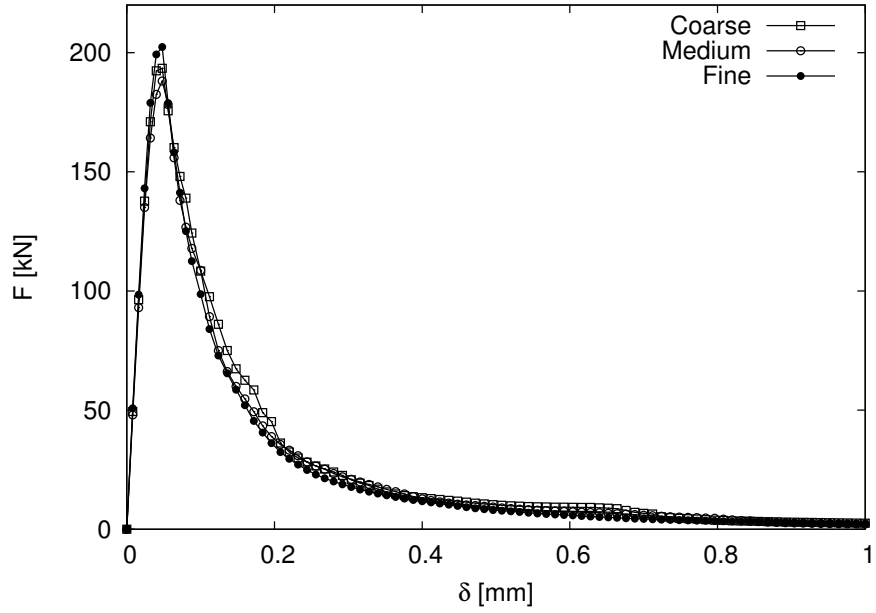


Figure 10: Load versus displacement for three lattices.

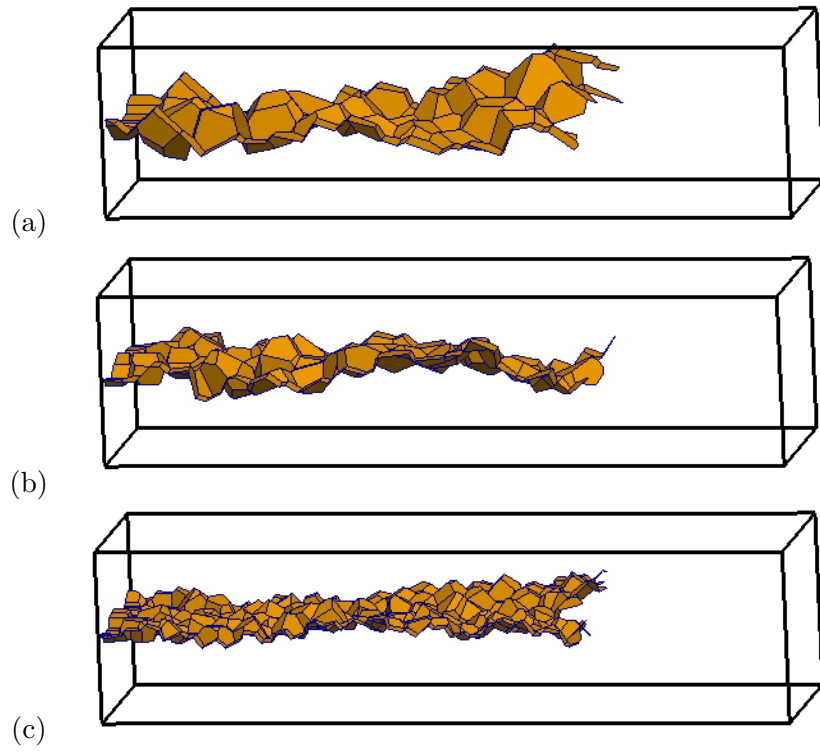


Figure 11: Crack patterns for (a) coarse, (b) medium and (c) fine lattice for a load point displacement of $\delta = 1.5$ mm in Figure 10. The shaded polygons represent the mid-cross-sections of elements with $\tilde{w}_c > 10 \mu\text{m}$.

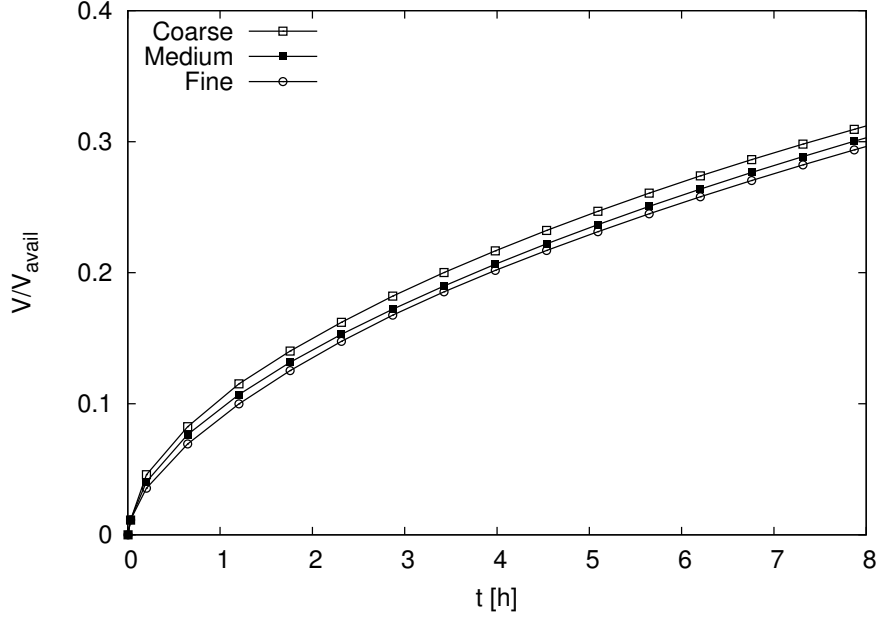


Figure 12: Influence of mesh size on the cumulative volume of inflow normalised by the domain volume.

However, the boundary and initial conditions, and the material input parameters, are changed so that the influence of fracture could be studied more effectively. On the left hand side of the model, the boundary is subjected to $P_c = 0$. Furthermore, the initial capillary pressure of all other nodes is set to $P_c = 1.736$ MPa, which for the chosen material parameters corresponds to an initial saturation of $S_{\text{init}} = 0.5$. Other input parameters for the transport problem are: $\alpha_0 = 1 \times 10^{-17} \text{ m}^2$, $\theta_s = 0.1$, $\theta_r = 0$, $a = 1$ MPa, $m = 0.5$ and $\xi = 0.001$. The transport analysis is performed for crack patterns obtained at a displacement of $\delta = 0.15$ mm in Figure 10.

Results for the cumulative volume of inflow at the left side of the specimen normalised by the available volume to be filled, from the time of initial wetting, are presented in Figure 12. The available volume to be filled is $V_{\text{avail}} = (1 - S_{\text{init}})\theta_s V_{\text{tot}}$, where V_{tot} is the total volume of the specimen. It can be seen that the inflow is practically independent of the element size.

Furthermore, contour plots of the capillary suction P_c are shown for the three lattices for the x-z plane (at $y = 0.125$ m) and for the x-z plane (at $x = 0.3$ m) in Figure 13. Darker regions correspond to lower values of capillary suction, which indicate higher amounts of intruded water. Slight broadening of the intrusion zone, lateral to the crack direction, is expected for the coarser

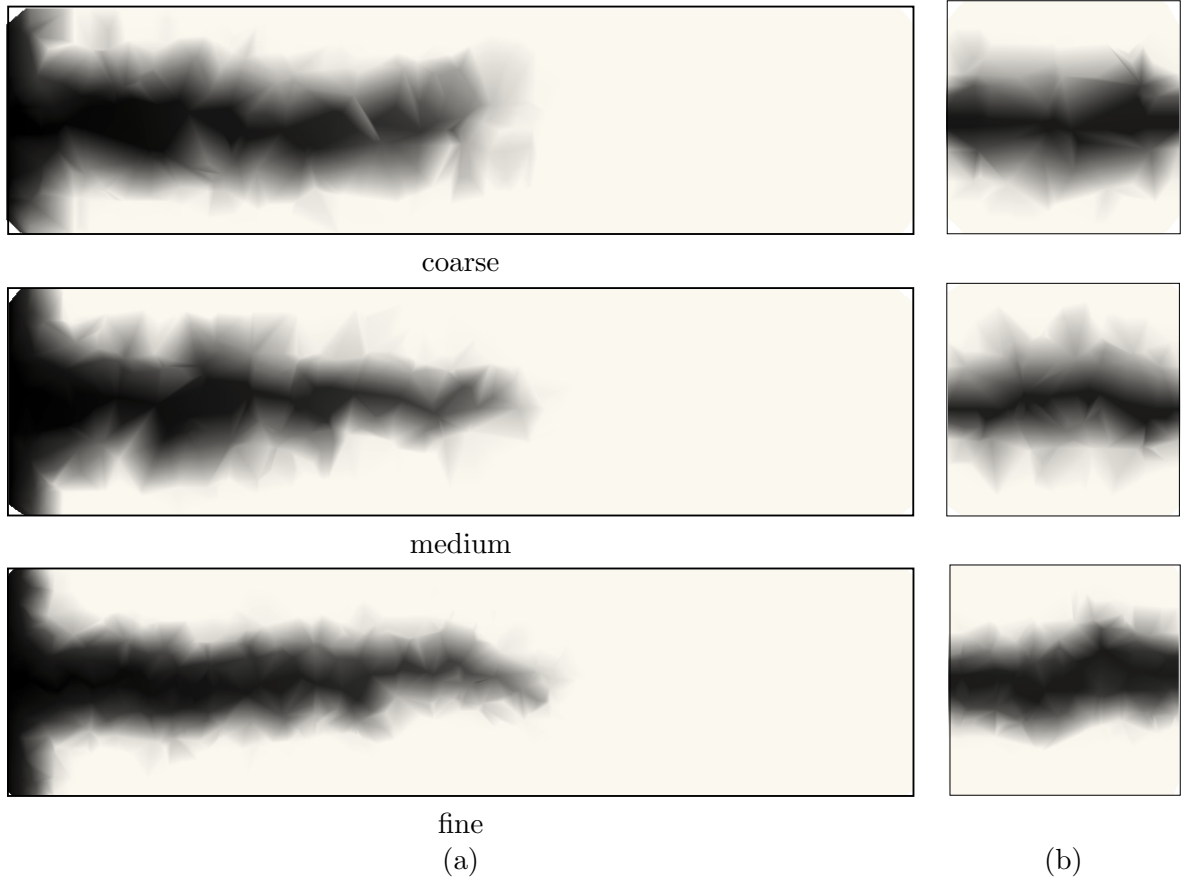


Figure 13: Contour plots of capillary suction P_c at 3.33 h for the (a) $x - z$ plane at $y = 0.125$ m and (b) $y - z$ plane at $x = 0.3$ m.

mesh design. Otherwise, the lattice model simulates the flow field mesh-independently.

4 Conclusions

This research extends the dual lattice approach for modelling crack-assisted mass transport in three dimensions. The Delaunay tessellation of an unstructured set of points defines the mechanical lattice, which represents material elasticity and fracture. The edges of the corresponding Voronoi diagram define the lattice of conduit elements, which simulate mass transport. A distinctive feature of the dual lattice approach is the alignment of conduit elements with potential pathways for crack propagation. Several benchmark comparisons have been presented involving non-stationary flow, fracture, and their coupling. The following conclusions and remarks can be made.

- Confirming the results of previous studies, random geometry lattices are effective in modelling cracking. There is no need to anticipate crack direction.
- The proposed discretisation scheme for the flow lattice facilitates the enforcement of boundary conditions. Local to a domain boundary, conduit elements have one node on the boundary and are directed perpendicular to the boundary.
- The lattice of conduit elements, defined by the Voronoi edges, is accurate and objective with respect to element geometry and size, as demonstrated through benchmark comparisons for non-stationary flow.
- The lattice of mechanical elements, defined by the Delaunay edges, is objective with respect to element geometry and size, as demonstrated through fracture simulations of double cantilever beams. The traction free condition is approached without stress locking.
- The proposed method for coupling the effect of crack opening, determined by the mechanical lattice, with transport properties of flow lattice yields objective results with respect to element geometry and size. This dual lattice approach facilitates the simulation of flow along crack paths and from crack faces into the bulk material.

The dual lattice approach presented herein is based on a one-way coupling of the mechanical and flow lattices. However, the approach can be developed to accommodate two-way coupling where the flow lattice results affect the mechanical response, as in hydraulically driven fracture. Other future work regards the simulation of coupled fracture-flow phenomena within heterogeneous materials in which multiple, interacting cracks are present.

5 Acknowledgements

P. Grassl acknowledges funding received from the UK Engineering and Physical Sciences Research Council (EPSRC) under grant EP/I036427/1 and funding from Radioactive Waste Management Limited (RWM) (<http://www.nda.gov.uk/rwm>), a wholly-owned subsidiary of the Nuclear Decommissioning Authority. RWM is committed to the open publication of such work in peer reviewed literature, and welcomes e-feedback to rwmfeedback@nda.gov.uk. The numeri-

cal analyses have been performed with OOFEM, an open-source object-oriented finite element program [18] extended by the present authors.

References

- [1] D. Asahina, J. E. Houseworth, J. T. Birkholzer, J. Rutqvist, and J. E. Bolander. Hydro-mechanical model for wetting/drying and fracture development in geomaterials. *Computers & Geosciences*, 65:13–23, 2014.
- [2] S. Berton and J. E. Bolander. Crack band model of fracture in irregular lattices. *Computer Methods in Applied Mechanics and Engineering*, 195(52):7172–7181, 2006.
- [3] J. E. Bolander and S. Berton. Simulation of shrinkage induced cracking in cement composite overlays. *Cement and Concrete Composites*, 26:861–871, 2004.
- [4] J. E. Bolander and S. Saito. Fracture analysis using spring networks with random geometry. *Engineering Fracture Mechanics*, 61:569–591, 1998.
- [5] J. E. Bolander and N. Sukumar. Irregular lattice model for quasistatic crack propagation. *Physical Review B*, 71, 2005.
- [6] B. Carrier and S. Granet. Numerical modeling of hydraulic fracture problem in permeable medium using cohesive zone model. *Engineering Fracture Mechanics*, 79:312–328, 2012.
- [7] G. Chatzigeorgiou, V. Picandet, A. Khelidj, and G. Pijaudier-Cabot. Coupling between progressive damage and permeability of concrete: analysis with a discrete model. *International Journal for Numerical and Analytical Methods in Geomechanics*, 29(10):1005–1018, 2005.
- [8] P. Grassl. A lattice approach to model flow in cracked concrete. *Cement and Concrete Composites*, 31(7):454–460, 2009.
- [9] P. Grassl and T. Davies. Lattice modelling of corrosion induced cracking and bond in reinforced concrete. *Cement and Concrete Composites*, 33:918–924, 2011.

- [10] P. Grassl and M. Jirásek. Meso-scale approach to modelling the fracture process zone of concrete subjected to uniaxial tension. *International Journal of Solids and Structures*, 47: 957–968, 2010.
- [11] P. Grassl, C. Fahy, D. Gallipoli, and J. E. Bolander. A lattice model for fracture and mass transport in concrete. In *Proceedings of Microdurability*, The Netherlands, 2012.
- [12] P. Grassl, C. Fahy, D. Gallipoli, and S. J. Wheeler. On a 2d hydro-mechanical lattice approach for modelling hydraulic fracture. *Journal of the Mechanics and Physics of Solids*, 75:104–118, 2015.
- [13] S. Marina, I. Derek, P. Mohamed, S. Yong, and E. K. Imo-Imo. Simulation of the hydraulic fracturing process of fractured rocks by the discrete element method. *Environmental Earth Sciences*, 73(12):8451–8469, 2015.
- [14] C. Miehe, S. Mauthe, and S. Teichtmeister. Minimization principles for the coupled problem of darcy-biot-type fluid transport in porous media linked to phase field modeling of fracture. *Journal of the Mechanics and Physics of Solids*, 82:186–217, 2015.
- [15] H. Nakamura, W. Srisoros, R. Yashiro, and M. Kunieda. Time-dependent structural analysis considering mass transfer to evaluate deterioration process of RC structures. *Journal of Advanced Concrete Technology*, 4:147–158, 2006.
- [16] A. Okabe, B. Boots, K. Sugihara, and S. N. Chiu. *Spatial tessellations: Concepts and applications of Voronoi diagrams*. Wiley New York, 2000.
- [17] M. Ortiz and A. Pandolfi. Finite-deformation irreversible cohesive elements for three-dimensional crack-propagation analysis. *International Journal for Numerical Methods in Engineering*, 44:1267–1282, 1999.
- [18] B. Patzák. OOFEM – an object-oriented simulation tool for advanced modeling of materials and structures. *Acta Polytechnica*, 52:59–66, 2012.
- [19] S. Roels, P. Moonen, K. De Proft, and J. Carmeliet. A coupled discrete-continuum approach to simulate moisture effects on damage processes in porous materials. *Computer Methods in Applied Mechanics and Engineering*, 195(52):7139–7153, 2006.

- [20] H. Sadouki and J. G. M. van Mier. Simulation of hygral crack growth in concrete repair system. *Materials and Structures*, 203:518–526, 1997.
- [21] T. Saka. *Simulation of reinforced concrete durability: dual-lattice models of crack-assisted mass transport*. PhD thesis, University of California, Davis, California, USA, 2012.
- [22] J. M. Segura and I. Carol. Coupled HM analysis using zero-thickness interface elements with double nodes. Part I: Theoretical model. *International Journal for Numerical and Analytical Methods in Geomechanics*, 32(18):2083–2101, 2008.
- [23] J. M. Segura and I. Carol. Coupled HM analysis using zero-thickness interface elements with double nodes. Part II: Verification and application. *International Journal for Numerical and Analytical Methods in Geomechanics*, 32(18):2103–2123, 2008.
- [24] M. Th. van Genuchten. A closed-form equation for predicting the hydraulic conductivity of unsaturated soils. *Soil Science Society of America*, 44:892–898, 1980.
- [25] B. Šavija, J. Pacheco, and E. Schlangen. Lattice modeling of chloride diffusion in sound and cracked concrete. *Cement and Concrete Composites*, 42:30–40, 2013.
- [26] L. Wang, M. Soda, and T. Ueda. Simulation of chloride diffusivity for cracked concrete based on RBSM and truss network model. *Journal of Advanced Concrete Technology*, 6(1):143–155, 2008.
- [27] P. A. Witherspoon, J. S. Y. Wang, K. Iawai, and J. E. Gale. Validity of cubic law for fluid flow in a deformable rock fracture. *Water Resour. Res.*, 16(6):1016–1024, 1980.
- [28] Y. Yao, L. Li, and L. Keer. Pore pressure cohesive zone modeling of hydraulic fracture in quasi-brittle rocks. *Mechanics of Materials*, 83:17–29, 2015.
- [29] M. Yip, J. Mohle, and J. E. Bolander. Automated Modeling of Three-Dimensional Structural Components Using Irregular Lattices. *Computer-Aided Civil and Infrastructure Engineering*, 20(6):393–407, 2005.